

# Disruption Mitigation by Massive Gas Injection in JET

M. Lehnen<sup>1†</sup>, A. Alonso<sup>2</sup>, G. Arnoux<sup>3</sup>, N. Baumgarten<sup>1</sup>, S.A. Bozhnikov<sup>4</sup>,  
S. Brezinsek<sup>1</sup>, M. Brix<sup>3</sup>, T. Eich<sup>4</sup>, S.N. Gerasimov<sup>3</sup>, A. Huber<sup>1</sup>, S. Jachmich<sup>5</sup>,  
U. Kruezi<sup>1</sup>, P.D. Morgan<sup>3</sup>, V.V. Plyusnin<sup>6</sup>, C. Reux<sup>7</sup>, V. Riccardo<sup>3</sup>, G. Sergienko<sup>1</sup>,  
M.F. Stamp<sup>3</sup> and JET EFDA contributors‡

*JET-EFDA, Culham Science Centre, OX14 3DB, Abingdon, UK*

<sup>1</sup>*Institute for Energy Research - Plasma Physics, Forschungszentrum Jülich, Association EURATOM-FZJ, Trilateral Euregio Cluster, 52425 Jülich, Germany*

<sup>2</sup>*Laboratorio Nacional de Fusion, Asociacion EURATOM-CIEMAT, Madrid, Spain*

<sup>3</sup>*Euratom/CCFE Association, Culham Science Centre, Abingdon, Oxon, OX14 3DB, UK*

<sup>4</sup>*Max-Planck-Institut für Plasmaphysik, EURATOM-Assoziation, D-85748 Garching, Germany*

<sup>5</sup>*Laboratoire de Physique des Plasmas-Laboratorium voor Plasmafysica, Association EURATOM-Belgian State, ERM/KMS, B-1000 Brussels, Belgium*

<sup>6</sup>*Instituto de Plasmas e Fusão Nuclear/IST, Associacao EURATOM-IST, Av. Rovisco Pais, 1049-001 Lisbon, Portugal*

<sup>7</sup>*CEA, IRFM, F-13108 Saint-Paul-lez-Durance, France*

**Abstract.** Disruption mitigation is mandatory for ITER in order to reduce forces, to mitigate heat loads during the thermal quench (TQ) and to avoid runaway electrons. A fast disruption mitigation valve (DMV) has been installed at JET to study mitigation by massive gas injection (MGI). Different gas species and amounts have been investigated with respect to timescales and mitigation efficiency. We discuss the mitigation of halo currents as well as sideways forces during vertical displacement events, the mitigation of heat loads by increased energy dissipation through radiation, the heat loads which could arise by asymmetric radiation and the suppression of runaway electrons.

## 1. Introduction

The mitigation of thermal and mechanical loads during disruptions is an urgent task to be solved for ITER to ensure the integrity of plasma-facing components (PFC). However, extreme loads are already an issue for present day machines like JET, with its new ITER-like wall, having the material used in ITER for DT operation [1]. The experiments reported here were performed in a full graphite environment in preparation of a potential mitigation system for the JET ITER-like wall.

Disruption mitigation has to fulfil three aims: *mitigation of forces* from halo and eddy currents, *mitigation of convective/conductive heat loads* during the thermal quench, *mitigation of heat loads from high-energy electrons*, so-called runaway electrons. The ITER mitigation system has to be capable of reducing the expected forces by a factor 2 – 3 and the thermal loads on Be and W components by at least a factor 10 to ensure integrity and lifetime of PFC [2, 3]. The generation of runaway electrons (RE) is of

† email: m.lehnen@fz-juelich.de

‡ See the Appendix of F. Romanelli et al., paper OV/1-3, this conference

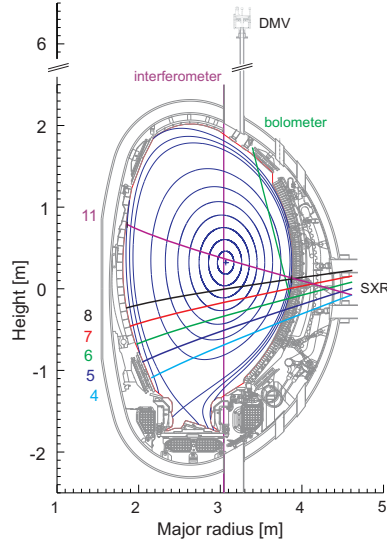


**Figure 1.** Set-up of the disruption mitigation valve at JET. The valve is situated at the end of a 4 m tube with 40 mm diameter. Equilibrium reconstruction for NBI heated pulse (Pulse No 77808). The lines of sight used for the estimate of the time of flight are given in green for bolometry and in magenta for interferometry. The SXR channels are used in section 2 to document the penetration of the cooling front.

special concern. Already at low RE currents of 0.5 MA a temperature rise on PFC of up to  $700^\circ$  has been observed in JET [4, 5]. RE currents in ITER are expected to reach up to 10 MA and would cause significant melting of PFC. Beside the efforts taken for disruption avoidance, two main mitigation techniques have been followed up so far as last resort in the case of an unavoidable disruption: massive gas injection and pellet injection. The latter was for some time regarded as not feasible because of low assimilation of material in the plasma. However, new concepts are developed to overcome this drawback [6]. Massive gas injection is presently the most explored technique and is studied at many tokamaks: Alcator C-mod [7], ASDEX Upgrade [8], DIII-D [9], JT60-U [10], MAST [11], TEXTOR [12] and Tore Supra [13].

A fast valve (Disruption Mitigation Valve - DMV) has been installed at JET to study disruption mitigation by massive gas injection [14, 15, 16, 17]. The valve is positioned on top of the machine and the gas is guided by a 4 m long tube to the plasma. Gas species investigated are helium, neon, argon and mixtures of these with 90% of deuterium as well as pure deuterium. With a volume of the injection chamber of  $0.65 \times 10^{-3} \text{ m}^3$ , a maximum pressure of 3.6 MPa and a total release of about 50% of the stored gas, up to  $2.5 \times 10^{23}$  particles can be injected, corresponding to about 100 times the electron content in the plasma.

The target plasmas studied here have low shaping with triangularity  $\delta = 0.24 - 0.29$  and elongation  $\kappa = 1.7$ , the equilibrium reconstruction is given in figure 1. We studied mainly MGI into ohmic plasmas and neutral beam heated H-mode plasmas with up to  $P_{NBI} = 18$  MW. The plasma current varied between  $I_P = 1.5$  MA to 2.5 MA, but

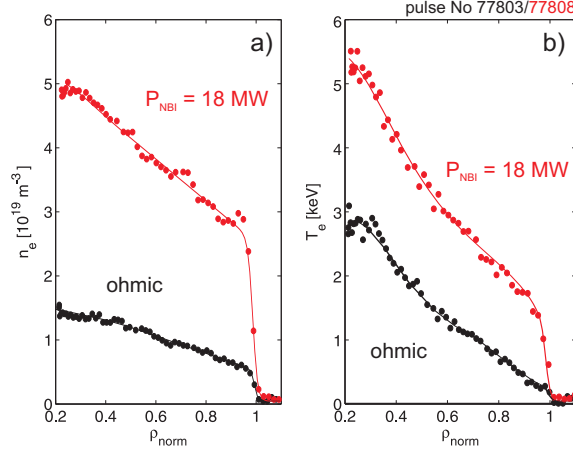


**Figure 2.** Electron density (a) and temperature (b) profiles for ohmic heating only and for  $P_{NBI} = 18$  MW (averaged over 0.5 s,  $I_P = 2.0$  MA,  $B_T = 3.0$  T).

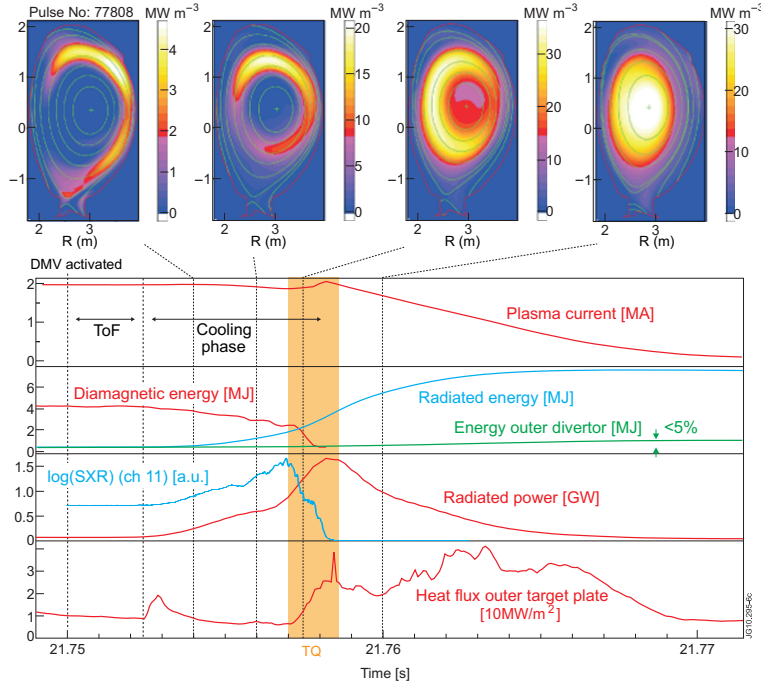


**Figure 3.** Disruption sequence. Ar/D<sub>2</sub> injection,  $p_{DMV} = 3.6$  MPa.

was set for most studies to  $I_P = 2.0$  MA. The toroidal magnetic field varied between  $B_T = 1.8$  T and 3.0 T. Typical density and temperature profiles as measured with high resolution Thomson scattering are given in figure 2.

Figure 3 shows the sequence of a typical JET disruption triggered by injection of about  $2 \times 10^{23}$  particles of the Ar/D<sub>2</sub> mixture into a NBI heated plasma. The disruption can be divided into three phases: pre-thermal quench (pre-TQ), thermal quench (TQ) and current quench (CQ). All disruptions described here were caused by MGI into a stable discharge with the exception of the vertical displacement events discussed in

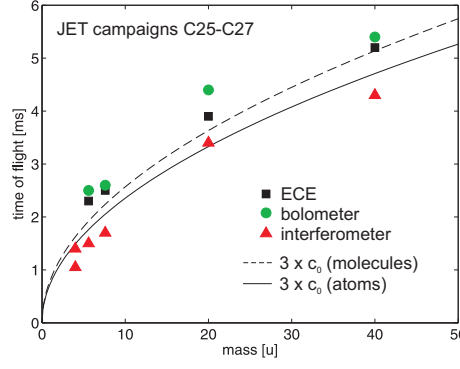


**Figure 4.** *Time of flight estimated from measurements of ECE, bolometer and interferometer.*

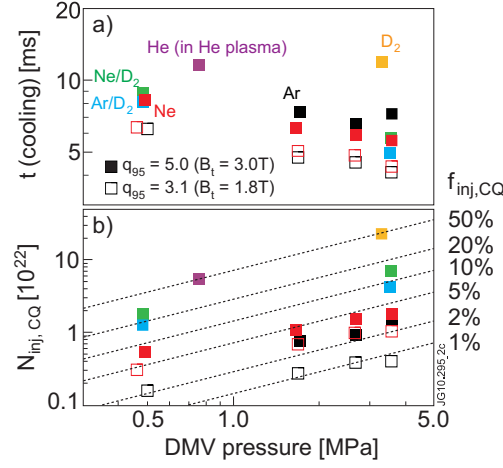


**Figure 5.** *Duration of the cooling phase (a) and calculated number of injected particles before the current quench (b) (ohmic plasmas, JET campaigns C25-C27).*

section 3. Accordingly, we define the pre-TQ phase to start with the activation of the valve. This phase includes the delay caused by the time of flight of the gas in the delivery tube and the subsequent cooling of the plasma edge. In the pre-TQ phase a significant part of the thermal energy is dissipated by line radiation. Eventually, the thermal quench sets in when the cooling front penetrated deeply enough to cause destabilisation of the plasma core and the remaining thermal energy is released within 1.5 ms as indicated by soft x-ray radiation (SXR). The thermal quench is followed by the decay of the plasma current caused by the high resistivity of the remaining low temperature plasma.

## 2. Pre-thermal-quench phase

The pre-thermal-quench phase includes the time-of-flight (TOF) of the gas from the valve to the plasma edge and the duration of the edge cooling process prior to the

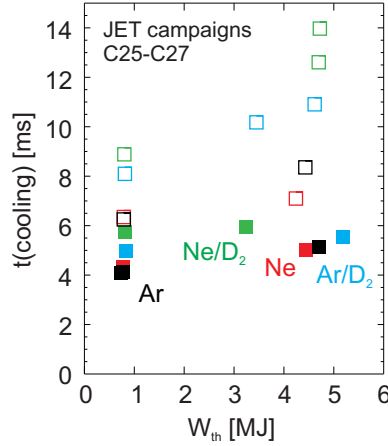


**Figure 6.** Duration of the cooling phase as function of stored thermal energy for  $p_{DMV} > 3$  MPa (closed symbols) and  $p_{DMV} < 1$  MPa (open symbols). Data for D<sub>2</sub> mixtures is for  $q_{95} = 5.0$  and data for pure gases is for  $q_{95} = 3.0$ .

initiation of the thermal quench (TQ). The TOF depends on the sound speed  $c_0$  of the injected species and thus mainly on the mass. From the theory of non-stationary adiabatic expansion into vacuum, the gas front arrives at the plasma edge after a time  $\Delta t = L/3c_0$ , where  $L = 4.5$  m and  $c_0 = \sqrt{\gamma RT/M}$ , with the adiabatic index  $\gamma$  being 7/5 for molecules and 5/3 for atoms. This theoretical TOF is compared in figure 4 with the experimental one found from different diagnostics. The outermost channel of the electron cyclotron emission radiometer (ECE) has been used to detect the first drop in temperature (see also [14]), the bolometry channel indicated in figure 1 has been used to detect the increase in radiation and the interferometer has been used to detect the first rise in electron density. All three diagnostics are toroidally 45° away from the position of the DMV. The time resolution of ECE and bolometry is 200  $\mu$ s, the time resolution of the interferometer is 10  $\mu$ s. The injected species are D<sub>2</sub> (M=4), 90%D<sub>2</sub>+10%Ne (M=5.6), 90%D<sub>2</sub>+10%Ar (M=7.6), Ne (M=20) and Ar (M=40). Although there is some systematic difference in the TOF found from these diagnostics, they all agree reasonably well with the theoretical prediction and we will use the theoretical TOF in the following analysis.

Figure 5a shows the cooling duration for various species and pressure. This time is defined as the delay between DMV activation and the start of the current quench (CQ) as indicated by the positive peak in the plasma current and includes therefore also the duration of the thermal quench. The TOF has been subtracted. The cooling duration decreases not only with the number of injected particles, but also with the safety factor  $q_{95}$ , indicating that the thermal quench is initiated when the cooling front reaches a critical flux surface (presumably  $q = 2$ ). Pure neon and argon as well as the mixtures with deuterium have a much shorter cooling duration compared to pure deuterium and helium. Due to technical reasons, helium injection was done only with helium plasma. However, injection of other species into helium plasma show that the timescales are

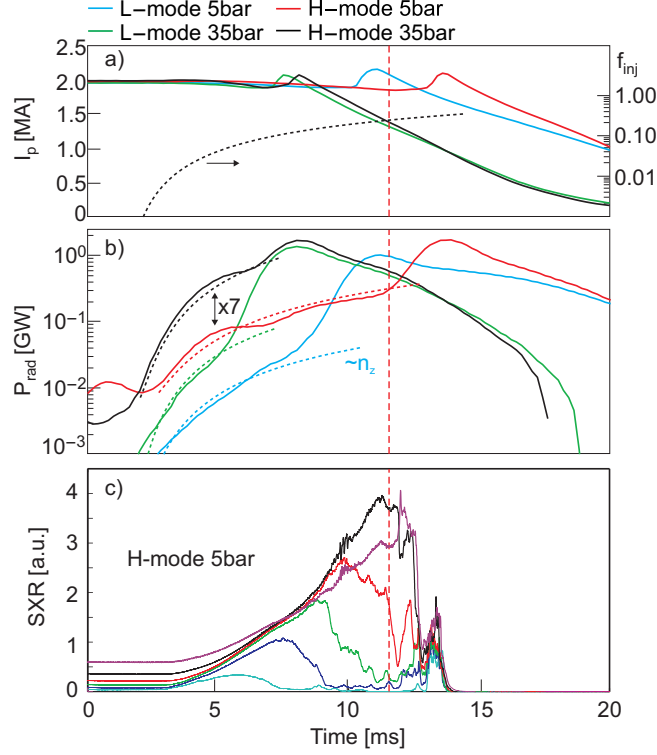


**Figure 7.** Plasma current (a) and radiation (b) during MGI for Ar/D<sub>2</sub> injection (Pulse Nos 76803/4, 76807/8). The dashed line in (a) gives the fraction of injected gas. The DMV is activated at  $t = 0$ . SXR data for the H-mode disruption at 0.5 MPa is given in (c). See figure 1 for colour coding.

determined by the injected species and not by the plasma species.

Beside the importance for the overall reaction time of the MGI system, the duration of the cooling phase has impact on the efficiency of the gas injection. The greater the quantity of injected gas, the shorter the pre-TQ phase and, therefore, less time is available for the gas injection. The assimilation of gas injected after the thermal quench is assumed to be much less efficient and is not contributing to the mitigation of heat loads during the TQ. Figure 5b gives the number of particles injected before start of the current quench  $N_{inj,CQ}$  as calculated from adiabatic expansion into vacuum. This approach has been validated with lab measurements using the JET set-up [18, 19, 20]. The fraction of gas injected before the current quench  $f_{inj,CQ}$  decreases with increasing pressure because of the shorter cooling phase. However, an increase in the absolute number of particles is still achieved.

It would be expected that the cooling duration increases with increasing stored energy. This is not generally the case as shown in figure 6. For injection of D<sub>2</sub> mixtures at low pressure, the cooling duration indeed increases with  $W_{th}$ . This is also the case, but less pronounced, for the pure gases. But for high pressure injection we find no dependence on the energy for all species. In order to analyse the cooling process in more detail, figure 7 shows the temporal evolution of the plasma current and the radiated

power during Ar/D<sub>2</sub> injection into L- and H-mode discharges, for the minimum and maximum pressure in the DMV. Although the waveform of the gas injection is identical for all four disruptions and, thus, is the amount of injected impurities, the radiated power  $P_{rad}$  is in the first phase of the cooling process more than one order of magnitude lower for the L-mode disruptions. This could be partly attributed to the low initial electron density, which is about 3 times higher in the H-mode cases. In this first phase,  $P_{rad}$  increases only linearly with the injected amount of gas as indicated by the dashed lines in 7b, which represent the fraction of injected gas  $f_{inj}$  times a factor to fit the measured  $P_{rad}$ . In the H-mode disruptions,  $P_{rad}$  increases proportional to the valve pressure by a factor 7, in L-mode the increase is about a factor 4. In the later phase of the cooling process a strongly non-linear increase of  $P_{rad}$  is observed about 1 – 2 ms before the current spike. The large difference in  $P_{rad}$  results in a comparable cooling duration for L- and H-mode with strong MGI ( $p_{DMV} = 3.5\text{MPa}$ ), despite the significant difference in thermal energy:  $E_{th} \approx 4.5\text{ MJ}$  (H-mode) /  $1.0\text{ MJ}$  (L-mode).

The penetration of the cooling front is illustrated in figure 7c, which shows an example of the development of the SXR emission during Ar/D<sub>2</sub> injection. The signal rises strongly during injection, which is typical especially for the injection of Argon, as the Bremsstrahlung increases significantly. As the cooling front penetrates into the plasma, a successive decay of SXR at the different measuring positions is observed (see figure 1 for the position of the SXR channels). Eventually, the cooling front reaches the critical surface and the thermal quench sets in. At that time the non-linear increase in  $P_{rad}$  sets in.

### 3. Mitigation of forces

Massive gas injection aims at a fast current decay in order to mitigate forces from halo currents. Figure 8 shows the linear current decay time extrapolated from the drop in current from 100% to 70% of the pre-TQ current and normalised to the plasma cross section. This definition has been chosen in order to avoid any influence from runaway current plateaux. In [21] it has been shown that the extrapolation range can have strong impact on the estimated decay time. Therefore, we compare in figure 8b with non-MGI references for both definitions, the more commonly used 80% to 20% decay and our definition. MGI causes a faster current decay in comparison to most reference disruptions. From the tendency of the standard definition to result in shorter  $\tau_{CQ}$  it becomes obvious that the CQ in many 'natural' disruptions starts with a slow current decay (most likely because of a weak impurity influx), which accelerates in the later phase of the CQ. With MGI, the current decay is fast from the very beginning of the CQ, which is essential for the mitigation of vertical displacement events (VDE). In order to keep forces from eddy currents tolerable, the current decay time has to stay above the lower bound of  $\tau_{CQ}/S = 1.7\text{ms/m}^2$  for ITER [22]. This limit was reached with pure Ar MGI in JET, however, the definition of  $\tau_{CQ}$  chosen here can lead to lower values compared to those from the 80% to 20% decay. For D<sub>2</sub> mixtures, where runaway

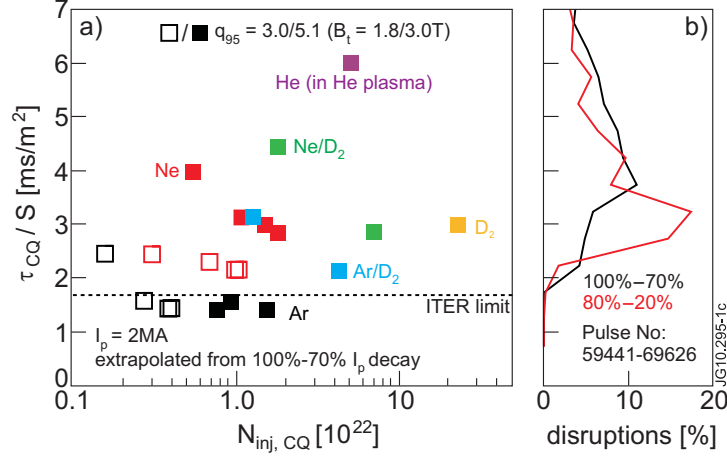


**Figure 8.** Linear current decay time for MGI during JET campaigns C25-C27 (a) and reference database (b).

generation is avoided, the difference between the two definitions amounts to about 20%. A saturation of  $\tau_{CQ}/S$  at larger numbers of injected particles is not obvious from the present database.

Halo currents can generate strong forces on the vessel and on inner wall structures. Especially, the product of halo current fraction  $I_{halo}/I_P$  and toroidal peaking factor  $TPF$  has to be limited to ensure the integrity of ITER wall components [23]. The halo current was measured at three toroidal positions and the TPF is defined as the ratio of the maximum to the average poloidal halo current. Halo currents are reduced by MGI, if the thermal quench is initiated before the vertical position has moved significantly in a VDE. Figure 9 shows time traces of deliberate VDEs, which were initiated by a vertical upward kick and a simultaneous switch-off of the vertical stabilisation. The red curves show data from a pure VDE without gas injection, the blue curves show data from a VDE during which the DMV was activated and injected Ar/D<sub>2</sub> with initial pressure of 3.2 MPa. The thermal quench was initiated at the same time for both cases, but the current quench was significantly accelerated with MGI. As a result the halo current was reduced by about a factor 2. Essential for a successful mitigation of halo currents is a fast reaction time. This time depends on the time of flight in the delivery tube and the duration of the cooling phase until thermal quench as described in section 2. Figure 10 shows the halo current fraction multiplied by the toroidal peaking factor as function of the delay between thermal quench and a vertical displacement of 10 cm for a fast VDE ( $\tau_{growth} \approx 5$  ms). The minimum reaction time of 7 ms, achieved with the Ar/D<sub>2</sub> mixture, allows a reduction of the halo currents by about 50%, assuming that a vertical displacement of 10 cm is taken as trigger for MGI and that control systems cause no further delay. Beside halo currents, sideways forces caused by toroidal asymmetries in the vertical current moment  $\delta M_z = \delta(I_p z_p)$  during the current quench are of concern for ITER [24, 25]. The normalised sideways impulse  $\int_{CQ} \delta M_z dt / 2I_p a_p$  (integrated over the current quench) is reduced by more than an order of magnitude (figure 10).



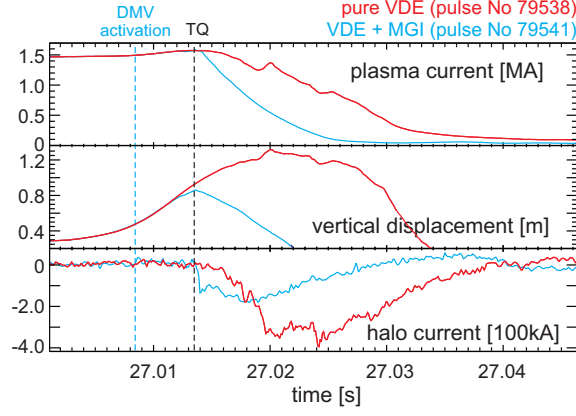


**Figure 9.** Evolution of deliberate VDEs: red curves are from a pure VDE and blue curves from MGI into a developing VDE where the current quench was initiated about 7 ms after  $t(\Delta z = 10 \text{ cm})$ .

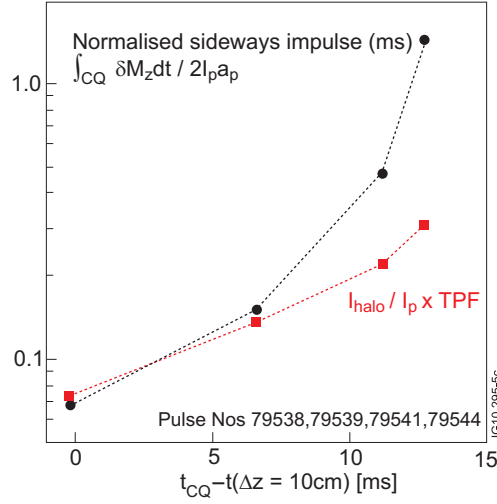


**Figure 10.** Reduction of halo currents and sideways forces.

## 4. Mitigation of heat loads

### 4.1. Heat loads by conduction/convection

Heat loads during the thermal quench can be reduced by enhancing the radiation with extrinsic impurities supplied by MGI. This is in contrast to many non-MGI disruptions, where the impurities are released not until the thermal quench and can therefore radiate only a minor fraction of the thermal energy. In order to quantify the fraction of radiated energy during the different phases of an MGI disruption, one has to carefully define the time windows of these phases. Another restriction arises from the time resolution of the bolometry, which can cause uncertainty during phases of fast rise in the radiated power as it happens in the thermal quench. In the following, we will analyse different approaches to quantify the fraction of radiated energy.

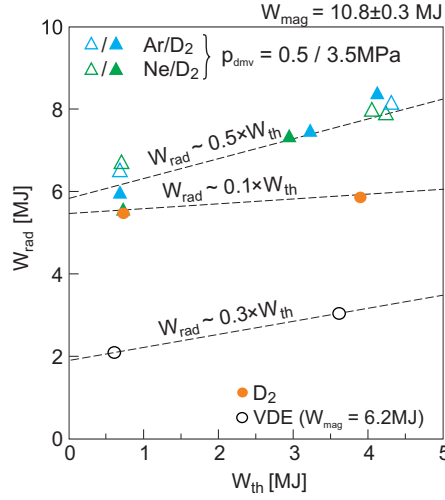


**Figure 11.** Energy radiated during the entire disruption (including pre-TQ, TQ and CQ phase) as function of initial stored thermal energy (JET campaigns C26-C27).

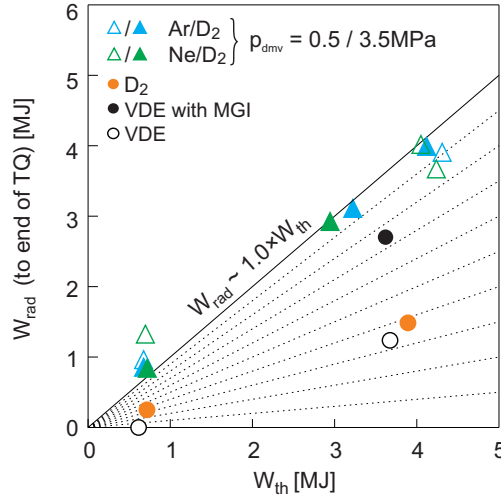


**Figure 12.** Energy radiated until the end of the thermal quench as function of initial stored thermal energy (JET campaigns C26-C27).

In order to avoid any uncertainties arising from the separation of the different disruption phases, an energy balance can be done by comparing the radiated energy during the whole disruption with the thermal and magnetic energy stored in the plasma before the disruption. The radiated energy is

$$W_{rad} = f_{ohmic} \times (W_{mag} - W_{mag}^{structure} - W_{mag}^{RE}) + f_{th} \times W_{th} , \quad (1)$$

where  $f_{ohmic}$  is the fraction of radiated ohmic energy and  $f_{th}$  is the fraction of radiated thermal energy. It was shown for JET non-MGI disruptions that almost 100% of the ohmic power generated during the current quench is dissipated by radiation [26] and we assume that  $f_{ohmic} \approx 1$  holds also for MGI. We analyse only disruptions without generation of runaways ( $W_{mag}^{RE} = 0$ ). In figure 11 the radiated energy is shown as

function of the thermal energy. The plasma current is 2 MA, the magnetic energy  $W_{mag} = 10.8 \pm 0.3$  MJ, accordingly. With the assumption that the dissipation of magnetic energy in the structure  $W_{mag}^{structure}$  is constant for these disruptions, we find that about 50% of the stored thermal energy is dissipated by radiation with Ar/D<sub>2</sub> and Ne/D<sub>2</sub>. For pure D<sub>2</sub> this fraction is only about 10%. Additionally, two data points from VDEs are shown in figure 11. They indicate a  $f_{th}$  of about 30%, which could be the result from the impurity release taking place before the thermal quench, when the plasma touches the upper dump plate [27]. The fraction of magnetic energy dissipated in the coils and vessel can be found from extrapolating to  $W_{th} = 0$ , which gives  $W_{mag}^{structure}/W_{mag} \approx 45 - 50\%$  for MGI. This is slightly higher compared to values of 25-45% found in previous studies on non-MGI disruptions [26, 28]. For the VDE  $W_{mag}^{structure}/W_{mag}$  is even higher, about 70%. It is important to keep in mind that this analysis is based on the assumption that  $W_{mag}^{structure}$  is constant when varying  $W_{th}$ , which might not necessarily be the case.

Previously, we defined the start of the current quench to be at the maximum current during the current spike. The end of the thermal quench can be assumed to coincide with this time. This is a practical definition, a more smooth transition from thermal quench to current quench is to be expected. The start of the thermal quench can be defined as the start of the decay in SXR from the plasma center. This is more reliable compared to the temperature drop measured by ECE, which is in many MGI disruptions already quite early in cut-off. With this definition of the start and end of the thermal quench, we find from figure 3 for the Ar/D<sub>2</sub> injection into H-mode that up to 50% of the thermal energy is lost predominantly by radiation before the TQ. About 40% of the remaining energy is radiated during the TQ. Thus, 30% of the initial energy would be lost by convection during the TQ. By divertor thermography, we find that typically only about 5% of  $W_{th}$  is found in the (outer) divertor [5].

Another and more precise definition for the end of the thermal quench can be used by taking the time where SXR emission is reduced to noise level. With this definition we see from figure 3 that more than 90% of  $W_{th}$  are radiated. Figure 12 shows the radiated energy until the end of the thermal quench using this new definition for the same data as presented in figure 11. For the deuterium mixtures we find now that about 90-100% of  $W_{th}$  is radiated. This fraction is independent from the pressure in the DMV, showing that already the maximum possible fraction of radiated energy is reached. Pure deuterium radiates only about 40% of  $W_{th}$  and VDEs are also in the same range. Injecting gas into a VDE raises the fraction to about 70-80%.

The uncertainty that arise from the latter technique is that during the thermal quench already part of the magnetic energy could be dissipated by radiation as the plasma starts to cool down. This might also explain, that values above 100% are found for low  $W_{th}$ . The method to integrate over the whole disruption implies the uncertainty that  $W_{mag}^{structure}$  might not be constant for different thermal energies.

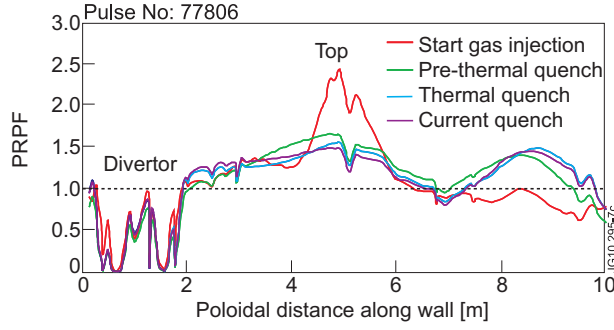


**Figure 13.** Poloidal radiation peaking factor (PRPF) during Ar/D<sub>2</sub> injection into H-mode plasma [27].

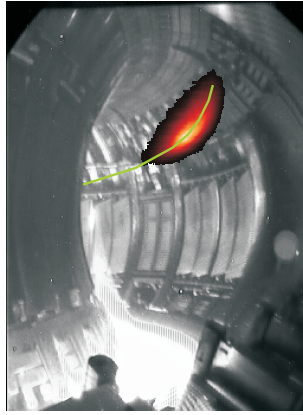


**Figure 14.** Fast camera image overlaid on an image of the vessel taken during the H-mode phase ( $t - t_0 = 6.9$  ms, Ne injection, pulse No 76321).

#### 4.2. Heat loads by radiation

Beside the heat loads caused by convection/conduction during the thermal quench, radiation could also lead to heat fluxes close to the PFC melting limits in ITER. During natural disruptions in JET, strong poloidal peaking of the heat fluxes by radiation have been reported, with peaking factor of up to 3.5 during VDE [27]. With MGI, the radiation is very localised in the early pre-TQ phase at the location the gas enters the plasma, but extends poloidally and toroidally in the later phase and generates a radiating mantle around the remaining core plasma just before the thermal quench (see figure 3). In the current quench, most of the radiation is found in the plasma center. The poloidal peaking factor of the heat flux at the wall caused by radiation is below 1.7 for most of the disruption phases (figure 13). A strong poloidal peaking of up to 2.5 is found in the pre-TQ phase. It has to be noted that the tomographic reconstruction of the radiation measured by bolometry is based on two cameras, which are  $\Phi = 90^\circ$  and  $\Phi = -135^\circ$  away from the injection port. Because the radiation spreads along the inclined field lines, it is expected that the radiation cloud is artificially broadened in poloidal direction, resulting in underestimated poloidal peaking factors.

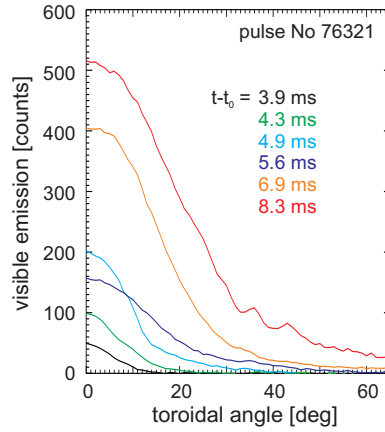


**Figure 15.** *Toroidal profiles of the visible emission at the injection port.*

In order to estimate the toroidal peaking, visible radiation recorded by a fast camera viewing the injection section has been analysed. An example of the visible emission in the range of about 400 – 700 nm as recorded by the fast camera during neon injection is shown in figure 14. The emission along the green line has been taken to reconstruct toroidal profiles. Figure 15 shows such profiles for different times after valve opening ( $t_0$ ) during neon injection at 1.7 MPa into L-mode plasma. Using simplifying assumptions, we can calculate an upper limit of the toroidal radiation peaking factor (TRPF). We assume that the total radiation consists only of visible emission, neglecting therefore the emission from ions with higher degree of ionisation, which have a broader distribution around the injection point. The bolometry, 90° toroidally separated from the injection port, measures a radiated energy during the pre-TQ phase equal to about 80 – 100% of the thermal energy loss. Radiation for  $\phi > 90^\circ$  is assumed to be zero. In contrast to the analysis of the poloidal profiles, only peaking of the emission profiles is considered, not the peaking of the resulting heat flux on the PFC. Integration of the emission along the line of sight has not been corrected.

Figure 16 shows the estimated toroidal peaking for L-mode and H-mode. During the initial phase with low radiation, the peaking factor is very high, reducing to 5 – 8 in the late pre-TQ phase, where the radiated power increased significantly. In this late phase a slight tendency towards lower TRPF for higher gas pressure and towards higher TRPF when going from L- to H-mode can be seen. Considering the method to determine the TRPF, this variation has to be taken with care and the TRPF derived here can only be used for a rough, upper limit estimate of the heat loads (see section 6.1).

## 5. Generation and mitigation of runaway electrons

Runaway generation is observed with injection of pure neon and argon. Argon injection leads for all possible gas amounts and for magnetic fields above 1.8 T to runaway currents

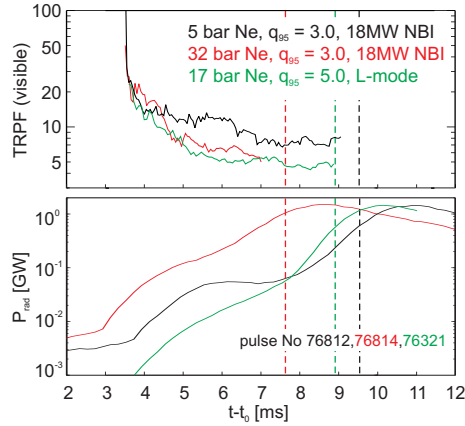


**Figure 16.** *Toroidal radiation peaking factor (TRPF) estimated from profiles of the visible emission during the cooling phase and radiated power measured at  $\Phi = 90^\circ$ . Vertical lines indicate TQ.*

of up to 50% of the initial plasma current. Traces of runaways indicated by neutron radiation can be found for Ar MGI even at magnetic fields down to 1.2 T. Runaway generation during Neon injection is much weaker and current plateaux are in most cases observed only in the tail of the current quench phase. No runaway generation is observed during injection of the deuterium mixtures, pure deuterium and helium.

It is assumed that in present-day tokamaks the primary runaway electrons during disruptions are mainly generated by the Dreicer mechanism ([29] and references therein). A second generation mechanism could be caused by the fast cooling during the thermal quench, and is referred to as hot tail generation [30]. In ITER additional sources of runaway electrons exists, which are independent from plasma density and electric field and can not be suppressed. The primary runaways are then multiplied by the avalanche process ([29] and references therein). Suppression of the Dreicer mechanism happens already at densities of the order of  $10^{20}\text{m}^{-3}$  in JET, whereas the suppression of the avalanche requires total electron densities (free and bound electrons) above  $n_c \approx 2 \times 10^{21}\text{m}^{-3}(1 + \bar{Z}/Z)^{-1} \times E/\text{Vm}^{-1}$ , where  $\bar{Z}$  is the mean charge state and  $Z$  the atomic number of the injected species [8, 31]. In this respect, we are interested to inject a high total number of electrons. Figure 17 is similar to figure 5b, with the difference that this time, the number of injected electrons  $N_{e,CQ}$  is plotted. Although Ne or Ar have a high atomic number, their slow delivery through the long tube, causes less electrons being injected compared to He or D<sub>2</sub>. But not only the number of injected electrons is of interest, also the assimilation in the plasma has to be sufficiently high to achieve relevant densities. Unfortunately, electron densities cannot be measured during the CQ by the interferometer in JET due to strong refraction. Also the impurity density in the current quench plasma  $N_Z(CQ)$  cannot be measured directly.

In order to get a rough estimate of  $N_Z(CQ)$  a simple zero dimensional model of the current decay has been applied (see also section 8). This model includes plasma current as well as the current induced in the structure, namely vacuum vessel and divertor

coils. The electron temperature of the current quench plasma is estimated from the power balance  $P_{rad} = P_{OH}$ . The impurity density is assumed to be constant during the current quench and is derived from fitting the measured current decay. The model can be applied only, if the radiation is predominantly caused by the injected species, which is expected for argon. Figure 18 shows the assimilation efficiency  $N_Z(CQ)/N_{inj,CQ}$  during Ar/D<sub>2</sub> injection into H-mode plasma heated by 18 MW of NBI. In order to investigate the dependency of the assimilation efficiency on plasma parameters, a scan of the plasma current has been performed either with constant  $B_t$  or with constant  $q_{95}$ . The uncertainty arising from the model is the unknown degree of current profile flattening during the thermal quench. This is reflected in the upper error bar indicating the range of values for different choices of internal inductance:  $l_i = 0.5$  and  $l_i = l_i^{pre-TQ}$ . The data shown in figure 18 shows an increase of the efficiency with lower  $q_{95}$ , whereas the plasma current has less impact on the efficiency if  $B_t$  is adjusted such to keep  $q_{95}$  constant. This dependence on  $q_{95}$  is consistent with what has been seen at DIII-D from direct density measurements [9]. However, it remains an open question if the flattening of the current profile shows a dependence on  $q_{95}$  as well, which could also partly explain the observed trend.

The fraction of critical density  $n_c$  achieved with Ar/D<sub>2</sub> and pure Ar injection is given in figure 19 as function of the injected amount of gas prior to the current quench. The current quench model shows that for the parameter range considered here, Ar is at least doubly ionised for plasma currents above 0.5 MA. We therefore assume  $\bar{Z}/Z = 2/18$  for Ar and fully ionised D<sub>2</sub> in the case of the deuterium mixture. Both, impurity density and electric field, have been derived from the model. The critical density  $n_c$  has been calculated from the maximum electric field at the start of the current quench. As the impurity density is assumed to be constant and the electric field decays during the CQ,  $n_e^{tot}/n_c$  increases during the CQ. The maximum electric field for  $l_i = 0.5$  ranges from 20 Vm<sup>-1</sup> to 27 Vm<sup>-1</sup> for Ar/D<sub>2</sub> and from 25 Vm<sup>-1</sup> to 39 Vm<sup>-1</sup> for pure Ar. The values taking  $l_i$  before the TQ are about 50-80% higher for ohmic pulses and 30% higher for the NBI heated cases. A clear increase of  $n_e^{tot}/n_c$  with the number of impurities injected can be seen. However, the electron density stays below 1% of  $n_c$ .

## 6. Discussion

In this section, we briefly discuss two import issues for ITER, the radiation load at the injection port and the suppression of the runaway avalanche. We also give a brief comparison to other work on MGI.

### 6.1. Heat loads from local radiation

Beryllium melting by local radiation at the injection port during the pre-TQ phase is of concern for ITER and could be the boundary condition determining the minimum number of injection ports necessary. The local heating of PFC in the vicinity of the

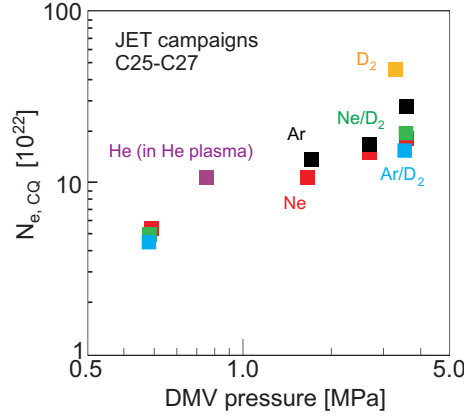


**Figure 17.** Number of electrons injected before the current quench ( $L$ -mode,  $q_{95} = 5.0$ ).

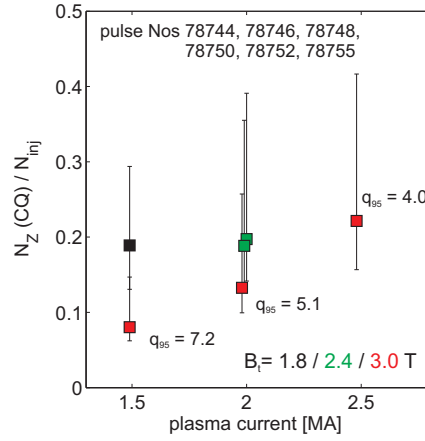


**Figure 18.** Assimilation efficiency with  $N_{inj}$  taken at the start of the thermal quench as indicated by SXR. The impurity density has been calculated by fitting the current from 100% to 60% of  $I_P(t = 0)$ . A flat current density profile and thus  $l_i = 0.5$  has been assumed. The upper error bar indicates the efficiency calculated for  $l_i$  values taken before the TQ, which are in the range of 0.7 to 0.9. The lower error bar indicates the efficiency with  $N_{inj}$  taken at the end of the thermal quench by assuming an average TQ duration of 1 ms. Ar/D<sub>2</sub> injection at 3.2 MPa, 18 MW NBI.

injection port in JET can be estimated from the peaking factors  $TRPF \approx 5.0$  and  $PRPF \approx 2.0$ , the energy loss in the pre-TQ phase of  $\Delta W_{pre-TQ} \approx 2$  MJ and the duration of the pre-TQ phase of  $\Delta t_{pre-TQ} \approx 5$  ms. The maximum heat load parameter from these numbers for JET is  $2 \text{ MJ m}^{-2} \text{ s}^{-0.5}$  translating into a temperature rise of about 150 K. Unfortunately, this estimated temperature rise cannot be confirmed by IR camera measurements as they are disturbed during the gas injection by radiation from the plasma itself. The present estimate for ITER for the pre-TQ phase is a loss of thermal energy of  $W_{pre-TQ} = 180$  MJ by radiation within 7 ms [2]. With toroidal and poloidal peaking factors of 5-8 and 2.0, respectively, we find a heat load parameter of  $40 - 64 \text{ MJ s}^{-0.5} \text{ m}^{-2}$  for a single injection point. The Be melting limit of



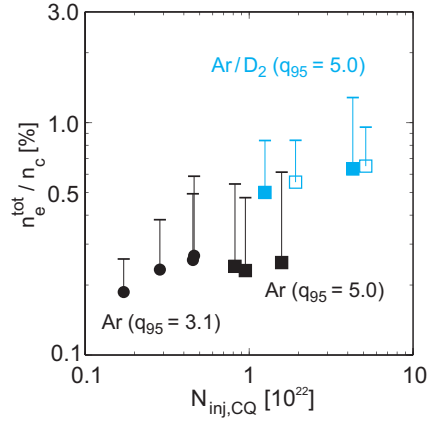


**Figure 19.** Total electron density normalised to the critical density for unconditional suppression of runaway electrons for different DMV pressure. The critical density has been calculated from the maximum electric field during the CQ. The electron densities have been calculated for  $l_i = 0.5$ , the error bar indicates the values for  $l_i$  taken before the TQ. Closed symbols - ohmic heating only, open symbols - 18 MW NBI, JET campaigns C26-C27.

about  $15 \text{ MJ s}^{-0.5} \text{ m}^{-2}$  suggests the use of at least 3-4 injection ports in ITER. A more precise analysis would require modelling of the toroidal spread of the radiation or direct measurements of toroidal profiles of the total radiation.

### 6.2. Suppression of the runaway avalanche

Suppression of the runaway avalanche requires significant higher densities than presently achieved in JET. As a consequence more gas has to be supplied on a shorter time scale. In order to illustrate the challenging requirements for such a gas injection system, we estimate the cooling duration  $\Delta t_{pre-TQ}$  from the simple assumption that the thermal quench is initiated after a certain energy  $W_{pre-TQ}$  has been dissipated by radiation:

$$W_{pre-TQ} = \int_0^{\Delta t_{pre-TQ}} P_{rad} \, dt. \quad (2)$$

Although the observation that the measured  $P_{rad}$  is proportional to the injected amount of impurities  $N_Z \sim p_{DMV} f_{inj}$  in the pre-TQ phase is not yet understood and needs further analysis, we take this relation for the following extrapolation from existing data. The calculated cooling duration  $\Delta t_{pre-TQ}$  is given in figure 20 as function of the pressure in the DMV. The two data points from Ar/D<sub>2</sub> injections show that the estimate is reasonable within this pressure range. Figure 20 shows that despite the shorter pre-TQ duration a further increase of the pressure will indeed raise  $N_{inj,CQ}$ . But this approach is technically limited. Further increase can only be achieved by enlarging the valve orifice and/or by a shortening of the distance between valve and plasma. An example with orifice diameter of 10 cm and only 1 m distance to the plasma edge is given in figure 20, showing that with this already demanding set-up an increase of  $N_{inj,CQ}$  by a factor 10 could be feasible, still not enough to reach the critical density in JET. However, this

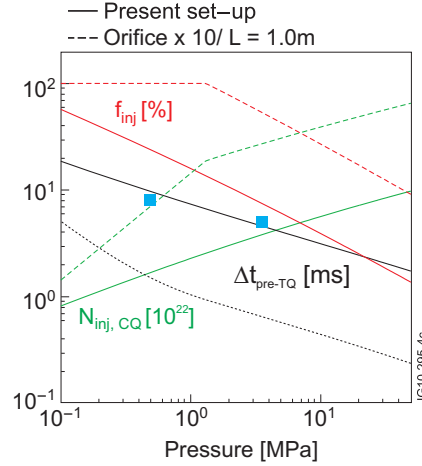


**Figure 20.** *Extrapolation of gas injection towards runaway suppression. Blue squares mark the measured  $\Delta t_{cooling}$  for Ar/D<sub>2</sub> (pulse Nos 77803/4).*

rough estimate is done on the basis that the relation  $P_{rad} \sim N_Z$  can be extrapolated to these amounts of gas, resulting in an extremely short pre-TQ phase in the sub-millisecond range. This might be a pessimistic assumption, because plasma parameters like the finite initial electron density might cause saturation in the radiated power. On the other hand we also don't know if the assimilation efficiency will not degrade with the number of injected particles.

Experiments with higher  $N_{inj,CQ}$  are urgently needed to draw a conclusion for ITER. But it becomes already obvious from the above calculations that the valve exit in ITER has to be close (of the order of a 1 m) to the plasma edge. Because of the neutron and gamma radiation loads, such a set-up is extremely challenging. JET data shows that the current decay rate with argon injection is already at the eddy current limit for ITER. A further increase in the injected amount of gas could imply further acceleration of the current quench and therefore lead to unacceptable forces. It remains an open question, if effects like opacity could prevent further acceleration of the current quench. If this is not the case, neon or deuterium mixtures might be the only candidates to avoid too fast a current quench.

### 6.3. Comparison to other work on MGI

*Halo currents* - It is common understanding from experiments with MGI as well as with pellets that a reduction of halo currents is achieved by a) initiating the thermal quench early during a VDE and b) by increasing the resistivity of the post-TQ plasma in order to accelerate the current decay. Experiments similar to what is reported in section 3 were done at DIII-D, where a threshold in vertical displacement was set to trigger the gas injection during a VDE [32]. These experiments show a maximum reduction by about a factor of 2 in both, the halo current fraction and the toroidal peaking, which gives a total reduction of  $I_H/I_P \times TPF$  similar to what is observed in JET. However

the reduction in JET is mainly due to a decrease in halo current rather than in TPF, which is already low for the unmitigated VDE ( $\sim 1.3$ ). Experiments at Alcator C-mod are consistent with these findings, they show a reduction of about a factor of 2 in halo current and also indicate a dependence on the injected species and therefore on the current decay rate [33]. With the ex-vessel valve of ASDEX Upgrade the reduction is also about a factor of 2, whereas the use of the in-vessel valve delivering a larger quantity of impurities to the plasma virtually fully suppresses halo currents [8].

*Heat Loads* - As described in section 4.1, a precise quantitative analysis of the radiated energy during the thermal quench is difficult. However, the data presented in figure 12 is in good agreement with work done at DIII-D: a radiative fraction in the range between 75% and 100% has been found for Ar, Ne and He, whereas injection of  $H_2$  or  $D_2$  shows a much lower fraction [9]. Nevertheless, in both experiments uncertainties arise from the challenge to precisely determine the length of the thermal quench and from the unknown fraction of radiated magnetic energy during this time. Especially, when considering the need to radiate at least 90% of the thermal energy in ITER, the accuracy of the present data is not sufficient to conclude that this goal can be achieved reliably. A high radiative fraction is supported by direct measurements of the heat flux to the divertor, which show a significant reduction with MGI. Data for example reported from DIII-D shows that the energy arriving in the divertor during the thermal quench initiated by Ne injection is less than 2% [34]. This is consistent with observations at JET, where the energy deposited in the outer divertor is of the order of a few percent for thermal energies in the range of 2.0 – 3.5 MJ. Unfortunately, only few examples are reported and a systematic analysis including a full energy balance which also takes into account main chamber fluxes has not yet been done.

*Runaways* - The goal with respect to runaway suppression is to achieve the critical density  $n_c$ . This density consists of free and bound electrons and there is no direct measurement of this quantity available. Therefore two practical approaches have been taken: measurements of free electrons by interferometry with short wavelength to avoid too strong refraction of the laser light (ASDEX Upgrade, DIII-D) and modelling of the measured current decay rate as described in section 5 (JET, TEXTOR). The latter is obviously no direct method, but also the first approach needs additional information, which is the degree of ionisation. With the assumption of singly ionised impurities, the highest fraction of  $n_c$  of about 24% has been achieved in ASDEX Upgrade with the in-vessel valve injecting about  $8 \times 10^{22}$  Ne atoms [8]. This refers to an assimilation efficiency  $N_Z(CQ)/N_{inj,CQ}$  of about 20% (assuming that all the gas is injected before the start of the CQ). In DIII-D fractions of  $n_c$  of up to 15% have been reported at an assimilation efficiency in the range of 10-20% [35]. The data presented in section 5 is in the same range, whereas that reported from TEXTOR ( $N_Z(CQ)/N_{inj,CQ} \approx 50\%$ , [18]) tends towards higher assimilation efficiencies. A direct comparison of both approaches is still pending. Despite a similar assimilation efficiency, the fraction of  $n_c$  that has been achieved in JET is much smaller compared to the other experiments. This is mainly due to the low fraction of gas being injected before the CQ because of the long distance

between valve and plasma.

## 7. Summary and conclusions

The experiments with massive gas injection at JET have shown that this concept is able to significantly reduce the loads during disruptions. Halo currents are reduced by up to a factor of 4, sideways forces even by more than a factor of 10 during VDE. The heat loads during the thermal quench can be reduced by the enhanced radiation. The fraction of radiated energy varies between 50% and almost 100%, depending on the analysis method. This uncertainty could be overcome by a full energy balance done either by including heat fluxes to the divertor and main chamber or by calculations of the magnetic energy dissipated in the surrounding structures. Runaway generation which can occur under certain conditions in non-mitigated disruptions in JET [4] could be avoided by injecting mixtures of Ne or Ar with 90% deuterium. Injection of these gas mixtures prevents from runaway generation by suppressing the Dreicer mechanism. However, a maximum of only about 1% of the critical density for the suppression of the runaway avalanche is achieved.

The optimum gas to be used for active disruption mitigation in JET with the present valve set-up is Ar mixed with 90% D<sub>2</sub>. This gas mixture provides a short time of flight of about 2 ms combined with a short cooling phase of about 5 ms with pre-pressure of 3.5 MPa and therefore a total reaction time of only 7 ms which is compatible even with fast VDEs. The fast current decay allows for efficient reduction of halo currents and sideways forces. This gas mixture also prevents from runaway generation and radiates a high fraction of the thermal energy. We have not discussed the impact of MGI on wall deconditioning and impurity contamination in the subsequent pulse. Work presented in [17] shows that mixtures with deuterium lead to wall loading with deuterium, resulting in a non-sustained breakdown for the pulse following the injection. There is also indication of an increased impurity concentration in the subsequent pulse and conditioning procedures might be necessary to reduce the impurity contamination. Therefore, it is necessary to have an advanced disruption detection scheme in JET to decide whether MGI is to be activated in a developing disruption or the disruption loads can be tolerated and mitigation is not needed.

This work was supported by EURATOM and carried out within the framework of the European Fusion Development Agreement. The views and opinions expressed herein do not necessarily reflect those of the European Commission.

## 8. Appendix - Current quench model

Impurity densities can be estimated from the current decay rate using a simple model. This model consists of equations for the plasma, vessel and divertor coil currents:

$$\underline{\underline{M}} \cdot \underline{\dot{I}} + \underline{R} \cdot \underline{I} = 0 , \quad (3)$$

with  $\underline{M}$  being the matrix of mutual and self inductances,  $\underline{R}$  the vector of resistances and  $\underline{I}$  the current in the various components, including the plasma itself. The plasma self-inductance is taken as

$$L_P = \mu_0 R \left( \log \frac{8R}{r} - 2 + \frac{l_i}{2} \right), \quad (4)$$

with major radius  $R$ , minor radius  $r$  and internal inductance  $l_i$ . The  $l_i$  after the TQ is difficult to determine and we therefore give error bars in figures 18 and 19 reflecting this uncertainty. Spitzer resistivity has been taken for the plasma resistance  $R_P$ . The current quench plasma temperature is defined by assuming that the ohmic power is fully balanced by radiation:

$$n_e n_Z L_Z(T_e) = \frac{R_P(T_e) I_P^2}{V_P}, \quad (5)$$

with plasma volume  $V_P$ , impurity density  $n_Z$  and impurity emissivity  $L_Z$ . The latter is taken from data derived from corona equilibrium [36]. This approach is reasonable as long as it is assumed that impurities enter the plasma during the TQ and that the fuelling efficiency during the CQ is negligible.

The inductance matrix for the four divertor coils and the vacuum vessel (for practical purpose being divided in 9 segments) has been derived by a finite-element solver and has been used for previous studies on the energy balance during disruptions [28]. In order to fit the measured vessel and divertor currents, a reduction of the mutual inductance between the plasma and the divertor coils by 20% and between the plasma and the vessel by 10% with respect to the values used in [28] was necessary.

The plasma current derived from equation 3 has been fitted to the measured current in the range 100% to 60% of  $I_P$  at the start of the current quench. An example is given in figure 21 assuming a homogenous current distribution after the thermal quench  $l_i = 0.5$ . In the late current quench the experimental data deviates from the model. This is attributed to a shrinking of the plasma cross-section due to vertical displacement and a resulting change in the plasma inductance which is not covered by the model. It is important to note that a substantial fraction of current is induced in the JET structure during the disruptions reported here. This significantly shortens the decay time of the plasma current and needs to be considered in order to have an accurate estimate of the electron temperature.

## References

- [1] G.F. Matthews et al., Phys. Scr. **T138** (2009) 014030
- [2] M. Sugihara et al., "Disruption and Runaway Electron Mitigation on ITER", 36th EPS Conference on Plasma Phys. Sofia, June 29 - July 3, ECA **33E**, P-4.165 (2009)
- [3] S. Putvinski et al., Fusion Energy 2010 (Proc. 23rd Int. Conf. Daejeon, 2010) (Vienna: IAEA) CD-ROM file ITR/1-6 and <http://www-naweb.iaea.org/naweb/physics/FEC/FEC2010/html/index.htm>
- [4] M. Lehnen et al., J. Nucl. Mater. **390-391** (2009) 740.
- [5] G. Arnoux et al., J. Nucl. Mater. **415** (2011) S817.
- [6] N. Commaux et al., Nucl. Fusion **50** (2010) 112001.

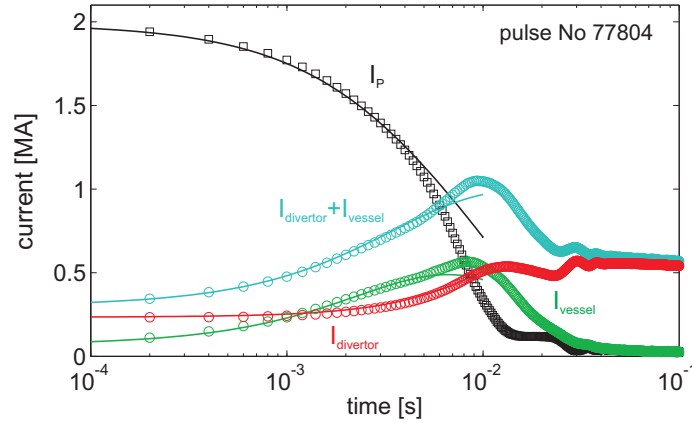


**Figure 21.** Current decay (symbols = experiment, lines = model). The data fit results in  $T_e(t=0) = 5.0\text{eV}$  and  $n_Z = 1.1 \times 10^{20}\text{m}^{-3}$  for  $l_i = 0.5$ .

- [7] D.G. Whyte et al J. Nucl. Mater. **363-365** (2007) 1160-7.
- [8] G. Pautasso et al., Plasma Phys. Control. Fusion **51** (2009) 124056.
- [9] E.M. Hollmann et al., Nucl. Fusion **48** (2008) 115007.
- [10] M. Bakhtiari et al., Nucl. Fusion **45** (2005) 318325.
- [11] A.J. Thornton et al., J. Nucl. Mater. **415** (2011) S836.
- [12] S.A. Bozhnikov et al., Plasma Phys. Control. Fusion **50** (2008) 105007.
- [13] C. Reux et al., Nucl. Fusion **50** (2010) 095006.
- [14] U. Kruezi et al., "Massive gas injection experiments at JET - performance and characterisation of the disruption mitigation valve", 36th EPS Conference on Plasma Phys. Sofia, June 29 - July 3, ECA **33E**, P-2.153 (2009).
- [15] M. Lehnen et al., "First experiments on massive gas injection at JET - consequences for disruption mitigation in JET and ITER", 36th EPS Conference on Plasma Phys. Sofia, June 29 - July 3, ECA **33E**, O-2.001 (2009).
- [16] S.A. Bozhnikov et al, "JET Experiments on Massive Gas Injection", 51st APS Meeting, Atlanta (2009), <http://meetings.aps.org/Meeting/DPP09/Event/110110>
- [17] U. Kruezi et al., J. Nucl. Mater. **415** (2011) S828.
- [18] S.A. Bozhnikov et al., "Massive gas injection experiments at JET - performance and characterisation of the disruption mitigation valve", 36th EPS Conference on Plasma Phys. Sofia, June 29 - July 3, ECA **33E**, P-1.180 (2009)
- [19] K.H. Finken et al., Nucl. Fusion. **51** (2011) 033007.
- [20] S.A. Bozhnikov et al., Nucl. Fusion. **51** (2011) 083033.
- [21] V. Riccardo et al., Plasma Phys. Control. Fusion **47** (2005) 117.
- [22] M. Sugihara et al., Nucl. Fusion **47** (2007) 337.
- [23] T.C. Hender et al, Progress in the ITER Physics Basis, Chapter 3: MHD stability, operational limits and disruptions, Nucl. Fusion **47** (2007) S128.
- [24] S.N. Gerasimov et al., "Scaling JET disruption sideways forces to ITER", 37th EPS Conference on Plasma Phys. Dublin, June 21 - June 25, ECA **34A** P4.121 (2010).
- [25] T.C. Hender et al., Fusion Energy 2010 (Proc. 23rd Int. Conf. Daejeon, 2010) (Vienna: IAEA) CD-ROM file EXS/10-3 and <http://www-naweb.iaea.org/napc/physics/FEC/FEC2010/html/index.htm>
- [26] J.I. Paley et al., J. Nucl. Mater. **337-339** (2005) 702.
- [27] A. Huber et al., J. Nucl. Mater. **415** (2011) S821.
- [28] V. Riccardo et al., Plasma Phys. Control. Fusion **44** (2002) 905.
- [29] P. Helander et al., Plasma Phys. Control. Fusion **44** (2002) B247.
- [30] H. Smith et al., Phys. Plasmas **12** (2005) 122505.

- [31] M. N. Rosenbluth and S. V. Putvinski, Nucl. Fusion **37** (1997) 1355.
- [32] D.G. Whyte et al., J. Nucl. Mater. **313316** (2003) 1239.
- [33] R. Granetz et al., Nucl. Fusion **46** (2006) 1001.
- [34] E.M. Hollmann et al., Nucl. Fusion **45** (2005) 1046.
- [35] E.M. Hollmann et al., Phys. Plasmas **17**, (2010) 056117.
- [36] H.P.Summers "The ADAS User Manual" (2004), version 2.6; <http://adas.phys.strath.ac.uk>